Radio Absorption in the Nightside Ionosphere of Mars During Solar Energetic Particle Events

Y Harada, Y Nakamura, B Sánchez-Cano, M Lester, N Terada, François Leblanc

Space Weather®

RESEARCH ARTICLE
10.1029/2023SW003755

Radio Absorption in the Nightside Ionosphere of Mars During Solar Energetic Particle Events

Y. Harada[1], Y. Nakamura[2], B. Sánchez-Cano[3], M. Lester[3], N. Terada[4], and F. Leblanc[5]

[1]Department of Geophysics, Graduate School of Science, Kyoto University, Kyoto, Japan, [2]Department of Earth and Planetary Science, Graduate School of Science, University of Tokyo, Tokyo, Japan, [3]School of Physics and Astronomy, University of Leicester, Leicester, UK, [4]Graduate School of Science, Tohoku University, Sendai, Japan, [5]LATMOS/CNRS, Sorbonne Université, UVSQ, IPSL, Paris, France

Key Points:

- Observations indicate a clear correlation between solar energetic particle fluxes and radio absorption in the nightside ionosphere of Mars
- The observed properties of radio absorption are well reproduced by a numerical model except for a factor of 3.7 systematic discrepancy
- Further model development and validation will pave the way for accurate prediction of the radio environment on the Martian surface

Correspondence to:
Y. Harada,
haraday@kugi.kyoto-u.ac.jp

Citation:
Harada, Y., Nakamura, Y., Sánchez-Cano, B., Lester, M., Terada, N., & Leblanc, F. (2023). Radio absorption in the nightside ionosphere of Mars during Solar Energetic Particle events. *Space Weather*, *21*, e2023SW003755. https://doi.org/10.1029/2023SW003755

Received 6 OCT 2023
Accepted 4 DEC 2023

Abstract Characterization, understanding, and prediction of the Martian radio environment are of increasing importance to the forthcoming human exploration of Mars. Here we investigate 3–5 MHz radio absorption in the nightside ionosphere of Mars caused by enhanced ionization at <100 km altitudes during solar energetic particle (SEP) events. We conduct a quantitative analysis of radio absorption and SEP flux data that have been accumulated by two spacecraft currently orbiting Mars, thereby demonstrating that radio absorption is clearly correlated with SEP fluxes. A comparison of the observations with radio absorption properties predicted by a numerical model indicates that the relative temporal changes, radio frequency dependence, and SEP energy dependence of the observed radio absorption are in agreement with the model prediction. Meanwhile, the model systematically overestimates the radio absorption in the ionosphere by a factor of 3.7. We explore several sources of uncertainty, including the electron-neutral collision frequency, absolute sensitivity of the SEP instrument, and limited transport of SEPs to the atmosphere, but the ultimate cause of the systematic discrepancy between the measured and modeled radio absorption is yet to be identified. Further efforts should be put into the development of a comprehensive and observationally validated model of radio absorption in the Martian ionosphere to assist the future crew and spacecraft activities on the surface of Mars.

Plain Language Summary Radio waves are widely used for communication, positioning, and navigation in our society. As human exploration of Mars progresses in the coming decades, radio technology will be in use for crew and spacecraft activities on the surface of Mars. On Earth, high-frequency radio communication is sometimes disrupted due to enhanced radio absorption in the lower ionosphere arising from solar flares. The ionosphere of Mars also causes strong radio absorption during space weather events as observed in the nightside ionosphere during solar energetic particle (SEP) precipitation. To assess the effects of ionospheric absorption on radio communication at Mars, we need to develop a reliable numerical model that is validated against observations. We initiate this effort by comparing observations with predictions from a state-of-the-art numerical model. The model successfully reproduces important aspects of the observed radio absorption during SEP events, namely relative temporal changes, radio frequency dependence, and SEP energy dependence. However, the modeled and observed absorption levels systematically differ by a factor of 3.7, reasons for which have not been fully understood. Further research is required to improve and validate the model if we are to characterize the radio communication environment prior to the future arrival of humans to Mars.

1. Introduction

Solar energetic particles (SEPs), which refer to high-energy solar particles accelerated during solar flares and at interplanetary shocks (e.g., Reames, 2013), have many profound effects on planetary environments as most extensively observed in geospace. Our neighboring planet, Mars, is no exception. For example, during the well-known September 2017 space weather event (see the *Space Weather Journal* special issue "Space Weather Events of 4–10 September 2017" (https://agupubs.onlinelibrary.wiley.com/doi/toc/10.1002/(ISSN)1542-7390.SW-SEPT2017) and the *Geophysical Research Letters* special issue "Impact of the Sept. 10, 2017, solar event on Mars" (https://agupubs.onlinelibrary.wiley.com/doi/toc/10.1002/(ISSN)1944-8007.MARS_SOLAR1)), SEPs and SEP-induced disturbances of the Martian space environment were observed by multiple spacecraft in orbit and on the surface of Mars (Ehresmann et al., 2018; Harada, Gurnett, Kopf, Halekas, Ruhunusiri, DiBraccio, et al., 2018; Lee et al., 2018; Ramstad et al., 2018; Sánchez-Cano et al., 2019; Schneider et al., 2018; Zeitlin et al., 2018). One of the most spectacular consequences of the SEP precipitation into the Martian atmosphere is

intense auroral emission from the entire nightside of Mars, termed "diffuse aurora," at peak emission altitudes of ~60 km (Schneider et al., 2015, 2018). The absence of a strong dipole magnetic field of internal dynamo origin enables the direct access of SEPs to the Martian atmosphere on a global scale as opposed to the terrestrial charged particle precipitation typically limited to high-latitude regions. Recently, a Monte Carlo model of SEP interaction with the Martian atmosphere developed by Nakamura et al. (2022) successfully reproduced the relative altitude profiles of the Martian diffuse aurora although there remains a factor of two discrepancy between the modeled and observed absolute intensities (the model overestimates the auroral emission intensity compared with the observation). The model results suggest a significant contribution of SEP protons to the emission peak in addition to SEP electrons that were initially postulated as the main driver of the Martian diffuse aurora (Schneider et al., 2015).

Another observable consequence of the SEP precipitation to the Martian atmosphere is the loss of trans-ionospheric high-frequency (HF) radar signals observed by orbiting spacecraft (Espley et al., 2007; Harada, Gurnett, Kopf, Halekas, Ruhunusiri, DiBraccio, et al., 2018; Lester et al., 2022; Morgan et al., 2010, 2014; Němec et al., 2014, 2015; Sánchez-Cano et al., 2019; Withers, 2011). The absorption of radio waves is caused by electron-neutral collisions in the lower (<100 km) ionosphere (Witasse et al., 2001). The "radar blackouts" provide an indirect proxy of electron densities in the lower ionosphere, which is difficult to access with in situ measurements. Until the arrival of the Mars Atmosphere and Volatile Evolution (MAVEN) spacecraft at Mars, it was challenging to conduct a quantitative comparison of the radio absorption with SEP fluxes because direct measurements of SEP energy spectra were not available in Mars orbit.

In the context of human and robotic exploration of Mars, the variability of the Martian space environment could have several relevant consequences analogous to the terrestrial space weather (e.g., Kataoka, 2022). Given the weak protection by the atmosphere and magnetic field of Mars, space radiation appears an obvious risk in terms of radiation exposure to humans. Another aspect of the Martian space weather is that ionospheric disturbances and enhancements possibly disrupt radio communication, positioning, and navigation activities on the surface of Mars. To first order, the ionospheric effects on positioning and navigation are expected to be limited because of the relatively small total electron content of the Martian ionosphere compared to the terrestrial ionosphere (Mendillo et al., 2004). Meanwhile, recent observations indicate the presence of ionospheric irregularities with a wide range of spatial scale lengths (Fowler et al., 2017, 2019, 2020; Gurnett et al., 2008; Harada, Gurnett, Kopf, Halekas, & Ruhunusiri, 2018; Mayyasi et al., 2019). The ionospheric irregularities at Mars could cause radio scintillation in principle but their significance is yet to be evaluated. Also, the radio absorption due to electron-neutral collisions in the lower ionosphere possibly leads to the loss of radio signals under enhanced ionization conditions. In this regard, it is worth noting that the Martian ionosphere acts as a strong HF radio wave absorber because of the large electron-CO_2 momentum transfer cross section (Nielsen et al., 2007).

Since MAVEN arrived at Mars, in situ SEP energy spectra have been nearly continuously monitored and the radar observations by the Mars Advanced Radar for Subsurface and Ionospheric Sounding (MARSIS) instrument on Mars Express (MEX) have been regularly conducted. As such, observational data that can directly relate the cause (SEP precipitation) and the effect (radio absorption) have been accumulated by the currently operating Mars orbiters to such an extent that has never been achieved at planets other than the Earth. Now that the planet Mars is a feasible and likely target of human exploration in the coming decades, characterization and understanding of the space weather and the radio communication environment of Mars are more relevant than ever before. Given the successful reproduction of the Martian diffuse aurora profiles by the new sophisticated numerical model (Nakamura et al., 2022), here we seek the feasibility of an application of the model to the assessment and prediction of the HF radio absorption environment for future crew and spacecraft activities on the Martian surface. Specifically, we quantitatively analyze the relationship between the radio absorption observed by MEX and SEP energy spectra observed by MAVEN and conduct a data-model comparison using the analyzed results and Nakamura et al. (2022)'s model prediction, thereby investigating the ability and limitation of the current model.

2. Observations

We analyze solar energetic particle data obtained by the MAVEN Solar Energetic Particle (SEP) instrument (Larson et al., 2015) (hereafter referred to as "MAVEN SEP" to distinguish from SEP particles) in combination with radar observations conducted by MARSIS on MEX (Jordan et al., 2009). MARSIS has two operational modes, the Active Ionospheric Sounding (AIS) and Subsurface Sounding modes, and we utilize both of them.

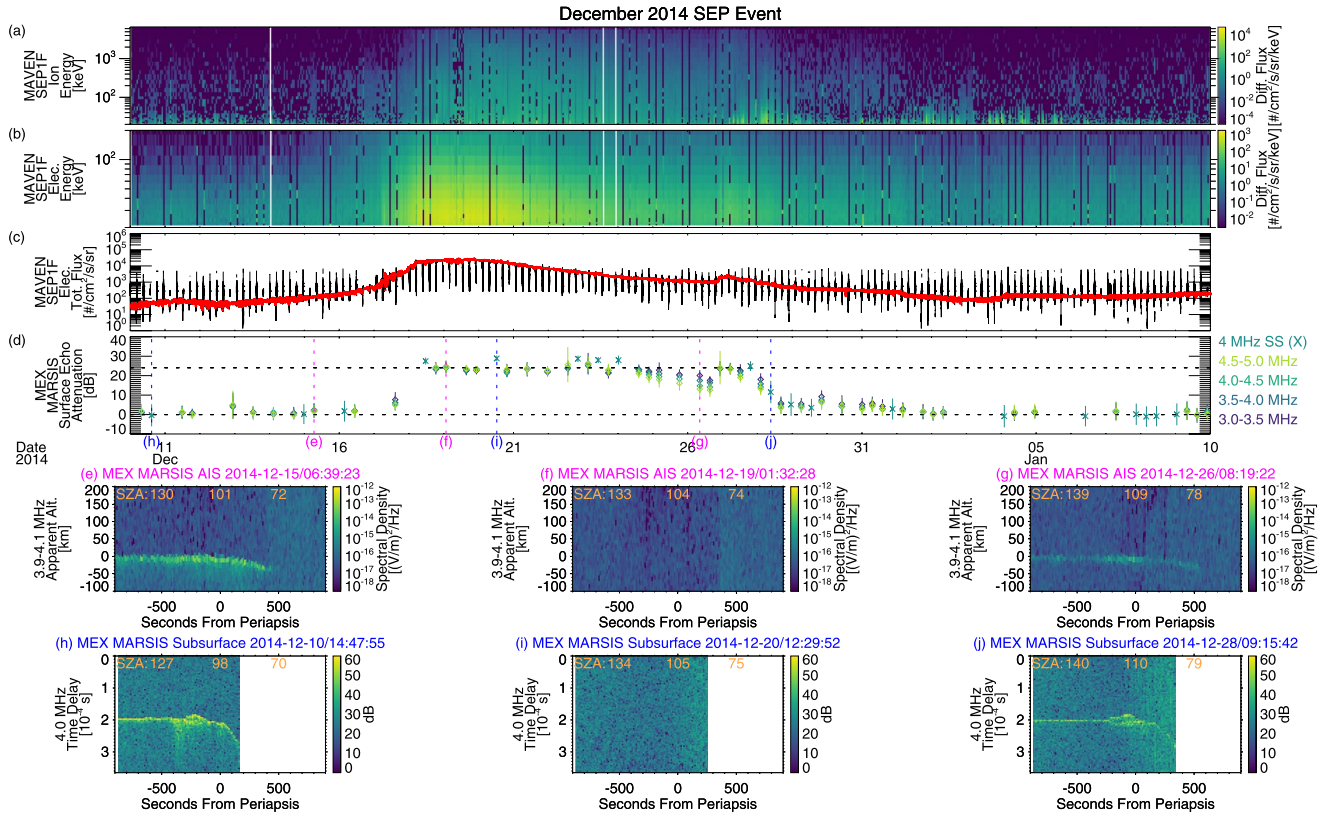

Figure 1. Mars Atmosphere and Volatile Evolution (MAVEN) Solar Energetic Particle (SEP) and Mars Express Mars Advanced Radar for Subsurface and Ionospheric Sounding (MARSIS) observations during the December 2014 SEP event. Energy spectra obtained by the (a) MAVEN SEP 1F ion channel and (b) MAVEN SEP 1F electron channel, (c) integrated total flux of the MAVEN SEP 1F electron flux (black) and filtered data (red, see text for the filtering criteria), (d) radio wave absorption derived from the surface echo attenuation observed by the MARSIS Active Ionospheric Sounding (AIS) (diamonds) and subsurface (X signs) modes (see Appendix A for the data processing procedures), and radargrams obtained by the MARSIS (e–g) AIS and (h–j) subsurface modes. The two horizontal dashed lines in panel (d) indicate the no absorption (0 dB) and estimated saturation (24.1 dB for the AIS mode operation at an altitude of 358 km (Nielsen et al., 2007)) levels for reference. The periapsis timings for panels (e–j) are indicated by the vertical dashed lines and text labels in panel (d). MEX's solar zenith angles are denoted in panels (e–j). Note that the MARSIS subsurface mode operates mainly on the nightside, leading to the data gap on the dayside as shown by the white areas in panels (h–j).

We first present case studies of two representative SEP events, namely the December 2014 and September 2017 events, for which MAVEN observed extensive diffuse aurora (Schneider et al., 2015, 2018) and detailed model-data comparison on the altitude profiles of auroral emission is conducted by Nakamura et al. (2022).

Figure 1 shows MAVEN SEP and MEX MARSIS observations during the December 2014 SEP event. The MAVEN SEP ion and electron energy spectra (Figures 1a and 1b) exhibit several orders of magnitude enhancement of the SEP flux starting from 16 December 2014 as documented in Lee et al. (2017). The black dots in Figure 1c show the MAVEN SEP electron total flux integrated over the measured energies (20–200 keV for electrons and 20–6,000 keV for ions). We observe spiky deviations that periodically appear at the orbital period (~4.5 hr), likely representing high noise floor when the attenuator is closed (upward deviations) and flux depletion around periapsis due to the particle loss into the atmosphere (downward deviations). To obtain the upstream SEP flux, we exclude the MAVEN SEP data when (a) MAVEN's altitude is lower than 1 Mars Radius or (b) the electron total flux is lower than 10^4 cm^{-2} s^{-1} sr^{-1} when the attenuator is closed. The red dots in Figure 1c show the electron total flux derived from the filtered data, demonstrating that the apparent deviations are successfully filtered out by this simple procedure. In the following analysis, we use the filtered MAVEN SEP data as the measured SEP fluxes to compare with the radio absorption.

Figure 1d shows radio wave absorption in the Martian nightside ionosphere derived from the surface echo attenuation observed by MEX MARSIS at each periapsis. The surface echo attenuation is derived by comparing the measured surface echo power at a given time to the nominal surface echo power expected for non-SEP event conditions. We describe the technical details of the data processing procedures in Appendix A. Each data point

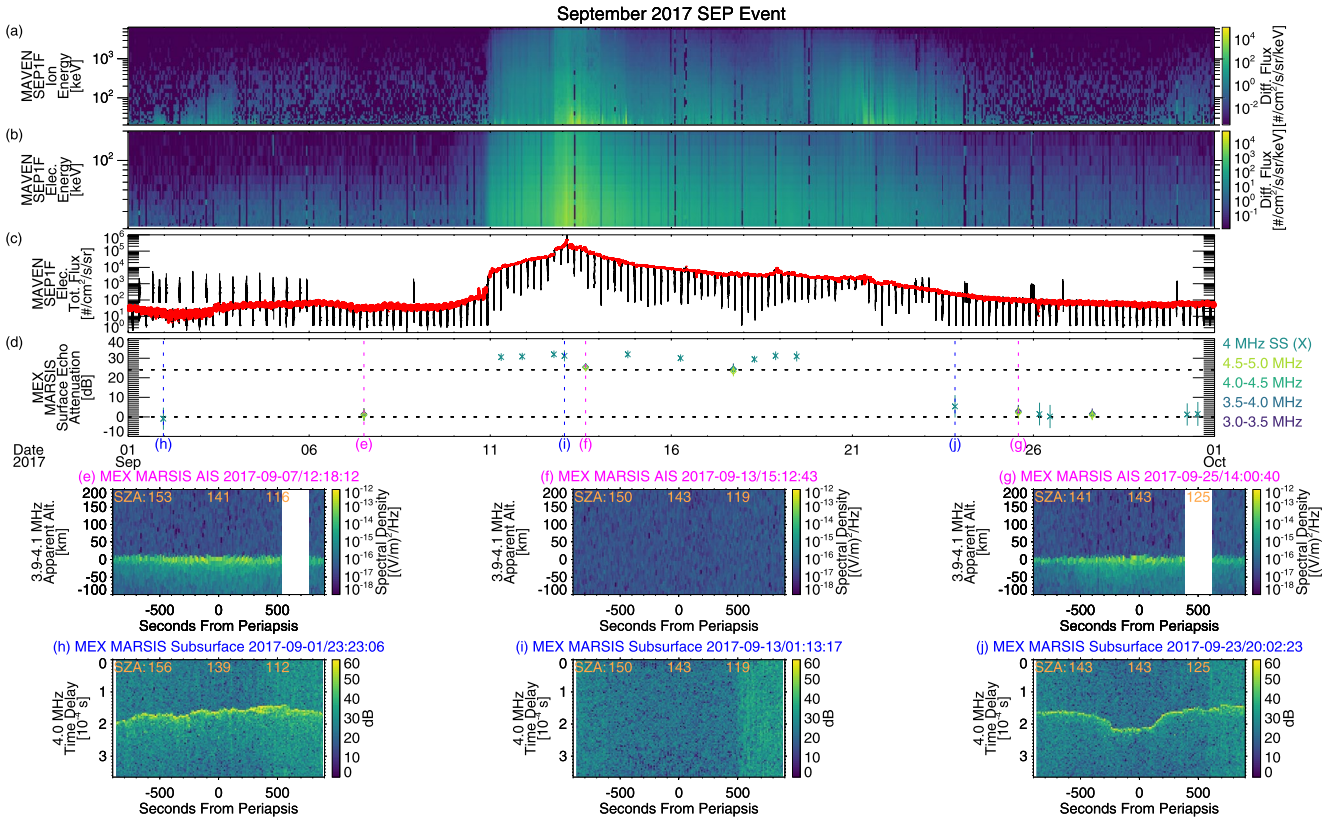

Figure 2. Mars Atmosphere and Volatile Evolution Solar energetic particle (SEP) and Mars Express Mars Advanced Radar for Subsurface and Ionospheric Sounding observations during the September 2017 SEP event in the same format as Figure 1.

and error bar in Figure 1d represent the average and standard deviation of the surface echo attenuation in each periapsis segment below 500 km altitude at solar zenith angle (SZA) > 100° for the two MARSIS operation modes: the AIS mode (shown by diamonds) and the subsurface mode (shown by X signs). We split the AIS ionogram data into four frequency ranges (3.0–3.5, 3.5–4.0, 4.0–4.5, and 4.5–5.0 MHz), while we use 4 MHz data for the subsurface mode. These frequencies are well above the typical critical frequency of <~1–2 MHz in the Martian nightside ionosphere (Němec et al., 2010). Figures 1e–1j present the AIS and subsurface mode radargrams obtained at representative timings. In the pre-SEP arrival, we observe clear surface echoes on the nightside (Figures 1e and 1h) and the near-zero absorption (at times labeled "(e)" and "(h)" in Figure 1d). Around the SEP flux peak, the surface echo completely disappears (Figures 1f and 1i) and the derived radio absorption is saturated (at the highest measurable level) as seen from the flat time series for each mode around times labeled "(f)" and "(i)" in Figure 1d. The observed AIS saturation level is consistent with the estimated saturation level of 24.1 dB at an altitude of 358 km for the AIS mode operation (Nielsen et al., 2007), which is indicated by the upper horizontal dashed line in Figure 1d. We note that the subsurface mode data seemingly have a higher saturation level, likely resulting from the higher time delay resolution and different data processing procedures (Appendix A). In the later phase with the moderate SEP flux, we observe weak surface echoes (Figures 1g and 1j) and the partial radio absorption (at times labeled "(g)" and "(j)" in Figure 1d). Remarkably, the partial absorption displays frequency dependence with stronger absorption at lower radio frequencies in the AIS data (at the time "(g)" in Figure 1d), which is consistent with the model prediction as described in Section 3.

Figure 2 presents radio wave absorption in the Martian nightside ionosphere during the September 2017 SEP event in the same format as Figure 1. The SEP flux enhancement at the peak (Figures 2a–2c) is more prominent than the December 2014 event. We observe an extended period of the saturated absorption (Figure 2d) with complete loss of the surface echo (Figures 2f and 2i) as documented in the literature (Harada, Gurnett, Kopf, Halekas, Ruhunusiri, DiBraccio, et al., 2018; Lester et al., 2022; Sánchez-Cano et al., 2019). Once the SEP flux diminishes, we observe a recovery of the surface echo (Figures 2g and 2j) to the pre-SEP state (Figures 2e and 2h).

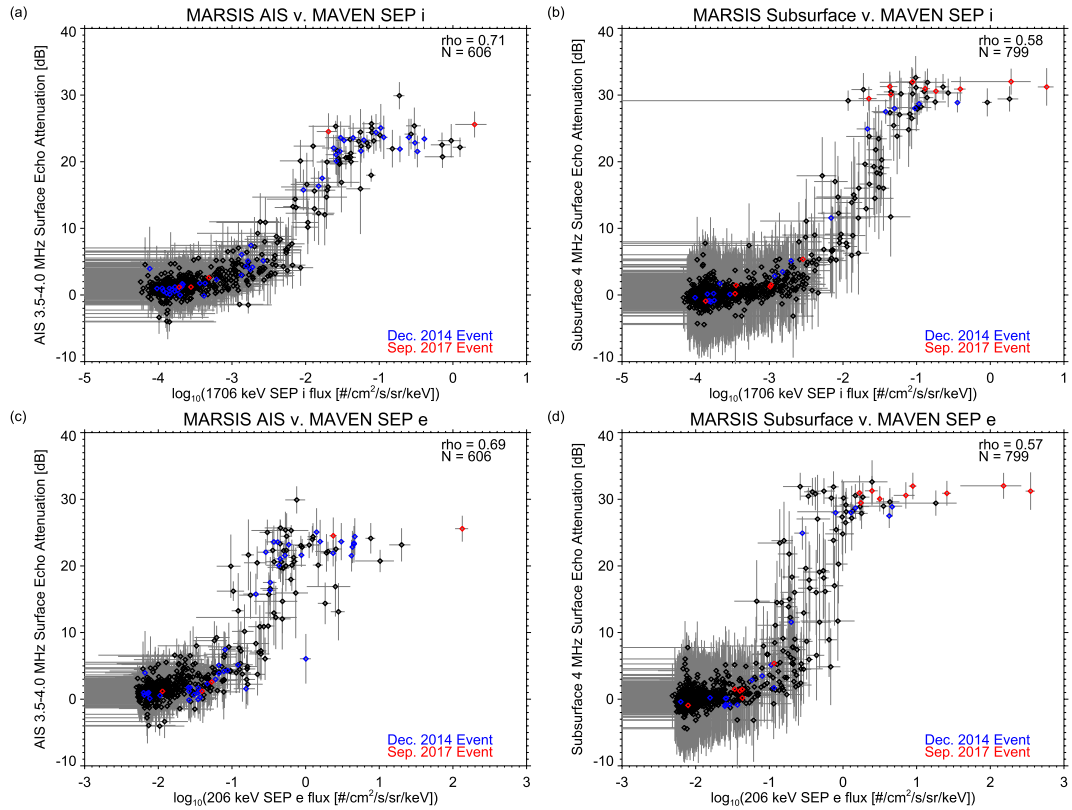

Figure 3. Scatter plots showing radar absorption derived from the Mars Advanced Radar for Subsurface and Ionospheric Sounding (MARSIS) (a, c) Active Ionospheric Sounding and (b, d) subsurface modes as a function of (a, b) 1.706 MeV Mars Atmosphere and Volatile Evolution (MAVEN) Solar energetic particle (SEP) ion flux and (c, d) 203 keV MAVEN SEP electron flux. The radio absorption is derived from MARSIS measurements below 500 km altitude at solar zenith angle > 100° for each periapsis, and each data point and error bar show the average and the standard deviation in the periapsis segment. For SEP flux, each data point and error bar show the average and the standard deviation of the measured SEP flux within ±3 hr of the Mars Express periapsis. The Spearman rank correlation coefficients ("rho") between the MAVEN SEP fluxes and the radio absorption as well as the number of data points ("N") are denoted in the upper right of each panel.

Overall, the analysis of the two SEP events demonstrates that the radio absorption in the nightside ionosphere of Mars measured by MARSIS varies in accordance with the SEP flux variations measured by MAVEN SEP.

We next expand the analysis to a larger set of data and conduct a statistical study. We analyze all the publicly available data obtained from 1 December 2014 to 31 December 2018, including other SEP events along with quiet intervals without any significant SEP fluxes. Figure 3 shows the radio absorption derived from the MARSIS AIS and subsurface data as a function of MAVEN SEP flux of 203 keV electrons and 1,706 keV ions. Each data point represents the radio absorption derived from MARSIS measurements below 500 km altitude at SZA > 100° for each periapsis (y-axis) and the measured SEP flux within ±3 hr of the MEX periapsis (x-axis). The entire data set (black) exhibits stronger radio absorption for higher SEP fluxes as seen in the representative cases of the December 2014 event (blue) and the September 2017 event (red). For these particle energies, the radio absorption displays clear dependence on the SEP flux with the Spearman rank correlation coefficients reaching 0.57–0.71. The AIS and subsurface mode radio absorption data show very similar behavior except for the aforementioned higher saturation level of the subsurface mode. Similar dependence is also found for the other radio frequencies of the AIS mode (not shown).

The degree of correlation between the radio absorption and SEP flux is found to be dependent on the SEP energy. Figure 4 shows the Spearman rank correlation coefficient as a function of SEP energy. The AIS and subsurface mode data again show generally similar behaviors, exhibiting stronger correlations at higher energies in the MAVEN SEP measured energy range. For electrons (red), we observe the strongest correlation at 200 keV which

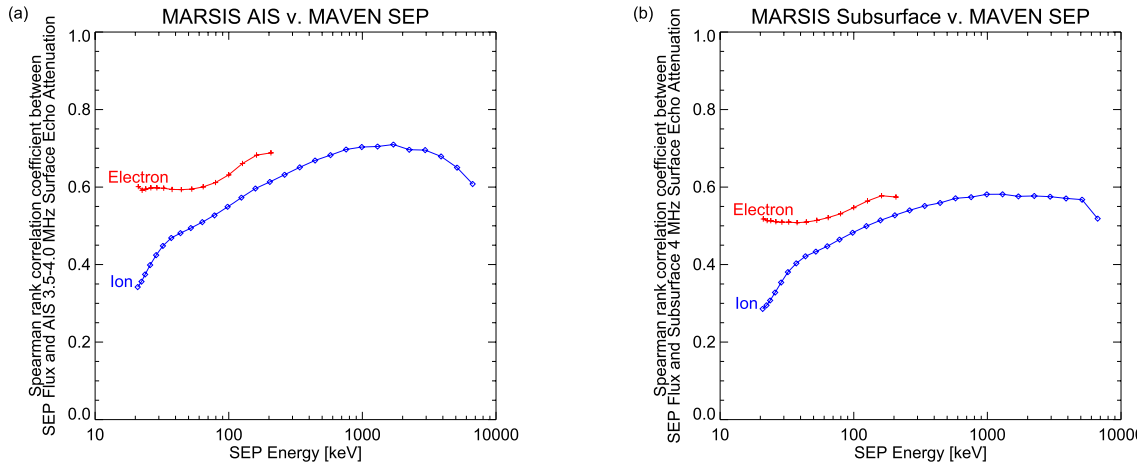

Figure 4. The Spearman rank correlation coefficients between the Mars Atmosphere and Volatile Evolution Solar Energetic Particle fluxes and the radio absorption derived from the Mars Advanced Radar for Subsurface and Ionospheric Sounding (a) Active Ionospheric Sounding and (b) subsurface modes as a function of particle energy.

is the highest measured energy. For ions (blue), the correlation coefficient increases monotonically with SEP energy and peaks out around ∼1–2 MeV.

3. Comparison With Model Results

This section compares the observed radio absorption with a model prediction for the December 2014 event, during which partial absorption was observed. We coupled the Particle TRansport In Planetary atmospheres (PTRIP) model (Nakamura et al. (2022)) and the Photochemical and RadiatiOn Transport model for Extensive USe (PROTEUS) (Nakamura, Terada, et al., 2023) to estimate the electron density profiles during the SEP event. PTRIP is a Monte Carlo model that solves the transport and collisions of incident energetic particles in the Martian atmosphere. For this study, the initial particle velocities are assumed to have an isotropic distribution over the hemisphere pointing down toward the planet, and we solved the three-dimensional equation of motion but only tracked the vertical location of the particles. PROTEUS is a one-dimensional photochemical model, which has been successfully applied to the Martian atmosphere (Nakamura, Leblanc, et al., 2023; Yoshida et al., 2023). PTRIP calculates the ion production rates, from which PROTEUS computes the ion and electron density profiles. The model inputs include electron and ion energy spectra fitted to MAVEN SEP measurements and the density profile of the neutral atmosphere of Mars from the Mars Climate Database (Millour et al., 2018). Figure 5a shows the altitude profiles of the CO_2, CO, N_2, O_2, O, H_2, H, and H_2O number densities used in the calculation. Those profiles except for H_2, H, and H_2O are used in PTRIP, and all the profiles are used as input in PROTEUS. In PROTEUS, we use chemical reactions listed in Nakamura, Leblanc, et al. (2023), which cover necessary neutral and ion chemistry induced by SEPs. Ionization sources other than SEPs are not considered in this study. Figure 5c presents an example of the computed electron density profile at 08:19:22 UTC on 26 December 2014 along with contributions from SEP protons (blue) and SEP electrons (red) separately.

Based on the computed electron density profile, we calculate the radio wave attenuation profile as well as the integrated total attenuation. As the radio wave propagates in the collisional ionosphere, each electron-neutral collision transfers some energy from the electromagnetic wave to the neutral thermal energy by converting the ordered momentum into the random motion of the neutral particles (Hunsucker, 1991). Radio wave attenuation in a collisional, non-magnetized plasma is given by

$$A = \frac{1}{2c\mu}\frac{\omega_N^2\,\nu}{\omega^2+\nu^2}, \tag{1}$$

where μ is the real part of the refractive index, ω_N is the electron plasma frequency, ν is the electron-neutral collision frequency, and ω is the radio wave angular frequency. For nondeviative absorption ($\mu \sim 1$), which is applicable to the low-altitude ionosphere of Mars, we obtain

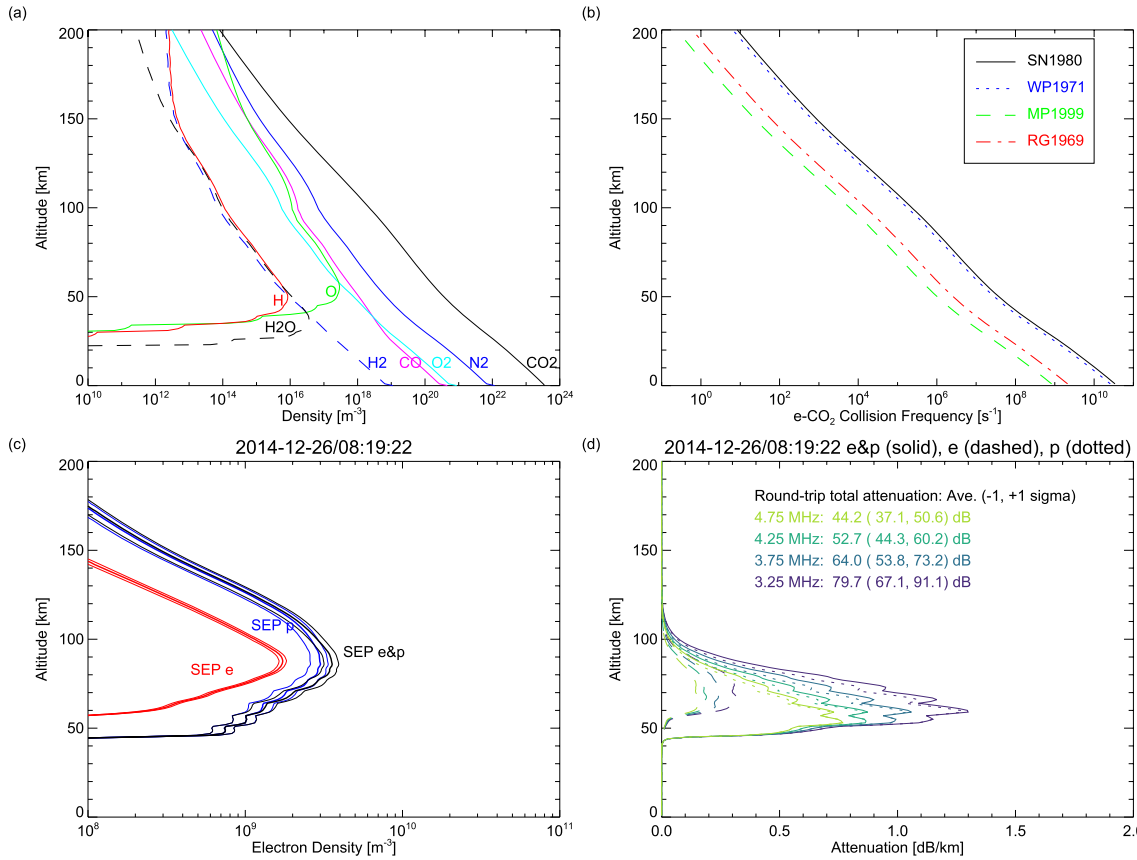

Figure 5. Altitude profiles of the model (a) input number densities of atmospheric species, (b) electron-CO_2 collision frequencies, (c) electron density, and (d) radio wave attenuation. In panel (b), four different expressions from Witasse et al. (2001) are shown: Schunk and Nagy (1980) based on Itikawa (1978) (SN1980); Whitten and Poppoff (1971) (WP1971); Melnik and Parrot (1999) (MP1999); and Rishbeth and Garriott (1969) (RG1969). The red, blue, and black lines in panel (c) represent Solar Energetic Particle (SEP) electron, SEP proton, and total contribution to the electron density profiles, respectively, and the thick and thin lines show the profiles with the average and ±1 standard deviation of the measured SEP flux within ±3 hr from 08:19:22 UTC on 26 December 2014. The dashed, dotted, and solid lines in panel (d) represent SEP electron, SEP proton, and total contribution to the radio wave attenuation profiles, respectively, and the text in the panel denotes the round-trip total attenuations derived from the average SEP energy spectra (and those from the average ±1 standard deviation in the parentheses) for different radio frequencies.

$$A \sim 4.61 \times 10^4 N_e \frac{\nu}{(2\pi f)^2 + \nu^2} \text{ [dB/km]}, \quad (2)$$

where N_e is the electron density (cm^{-3}), ν is the momentum-transfer electron-CO_2 collision frequency (s^{-1}), and f is the radio wave frequency (s^{-1}) (Hunsucker, 1991; Nielsen et al., 2007; Sánchez-Cano et al., 2019). For a given radio frequency f, we can compute the altitude profile of A from those of N_e and ν. We note that the specific attenuation (A/N_e) maximizes at the altitude where $\nu = 2\pi f$.

For the electron-CO_2 collision frequency, ν, Witasse et al. (2001) tested four expressions found in the literature and demonstrated that the choice of different formulations can introduce nontrivial differences in the calculated attenuation results. Specifically, they used: $\nu = 3.68 \times 10^{-14}(1 + 4.1 \times 10^{-11}|4{,}500 - T_e|^{2.93})N$ from Schunk and Nagy (1980) based on Itikawa (1978) (SN1980); $\nu = 8 \times 10^{-14}N$ from Whitten and Poppoff (1971) (WP1971); $\nu = 2.12 \times 10^{-16}\, T_e^{0.5} N$ from Melnik and Parrot (1999) (MP1999); and $\nu = 5.4 \times 10^{-16}\, T_e^{0.5} N$ from Rishbeth and Garriott (1969) (RG1969), where N is the CO_2 density (m^{-3}) and T_e is the electron temperature (K). Figure 5b shows the electron-CO_2 collision frequency profiles calculated from these expressions for the CO_2 density profile shown in Figure 5a. Here the electron temperature is assumed to be the same as the neutral temperature, which is reasonable at relatively low altitudes (say, below 100 km) relevant to radio absorption. As noted by Witasse et al. (2001), the first two expressions and the last two expressions show significantly different results and are fundamentally different in nature; SN1980 and WP1971 are based on experimental results while MP1999 and RG1969 are based on the hard sphere collisions model. Witasse et al. (2001) recommend the experimental values

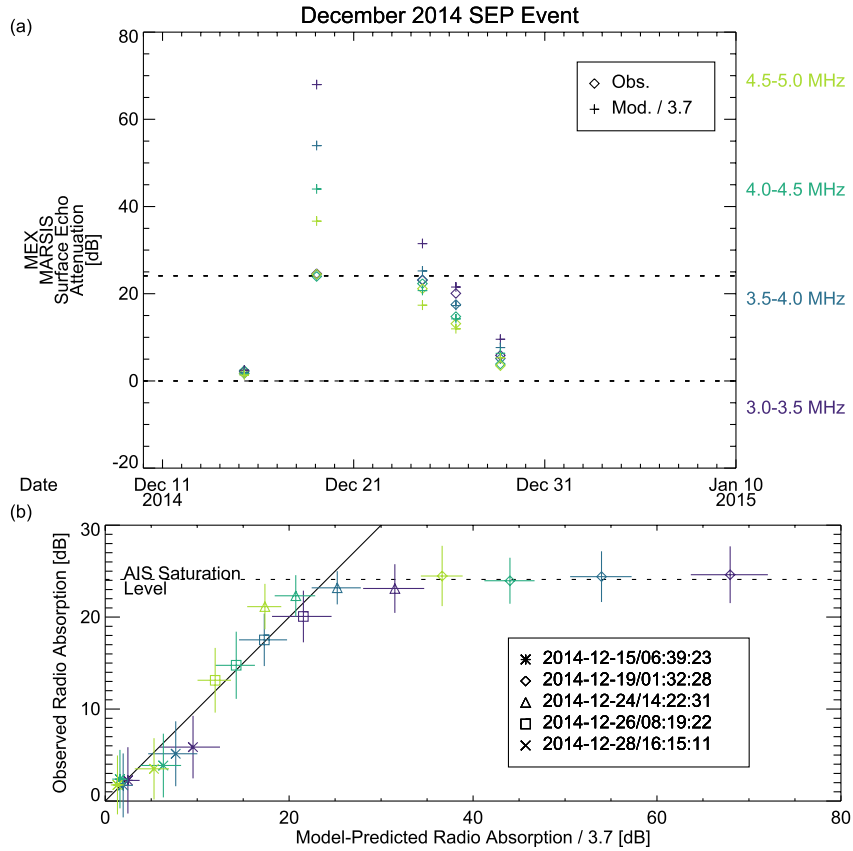

Figure 6. (a) Time series and (b) scatter plot of model-observation comparison of radio absorption for five selected periapses during the December 2014 solar energetic particle (SEP) event. In both panels (a, b), the observational data points represent the average radio absorption observed below 500 km altitudes at solar zenith angle (SZA) > 100° for each periapsis and the model data points represent the model-predicted absorption divided by an arbitrary constant factor of 3.7. In panel (b), the horizontal error bars represent the variability range of ±1 standard deviation of Mars Atmosphere and Volatile Evolution SEP energy spectra used in the model, while the vertical error bars represent the standard deviation of the radio absorption observed below 500 km altitudes at SZA > 100° for each periapsis. The horizontal dashed line at 24.1 dB indicates the estimated saturation level (Nielsen et al., 2007) for reference.

of SN1980 and WP1971, which differ only by ~20%–30% from each other. Hence, we chose the widely used SN1980 values in the following calculation.

Figure 5d shows the calculated attenuation profile from Equation 2 with the SN1980 collision frequency formulation. The predicted attenuation occurs mainly at low altitudes below 100 km with a peak around ~50–60 km altitudes. Since the ionization is caused predominantly by SEP protons below ~85 km altitudes (Figure 5c), the SEP proton-induced attenuation (dotted lines in Figure 5d) is overall much stronger than the SEP electron-induced attenuation (dashed lines in Figure 5d). By integrating the attenuation profile over altitudes and doubling it, we derive the round-trip total attenuation as denoted by numbers in Figure 5d, which can be directly compared to the observed attenuation by MARSIS. We point out that the predicted attenuation is stronger for lower radio frequencies in qualitative agreement with the observations.

We compute the electron density profiles based on the MAVEN SEP measurements for five selected MEX periapses during the December 2014 SEP event, thereby deriving the model-predicted radio attenuation. Figure 6 presents the direct comparison between the model prediction and the MARSIS observations except that the model prediction is reduced by an arbitrary constant factor of 3.7. The arbitrarily reduced model results remarkably agree with the observations below the AIS saturation level, suggesting that the model adequately reproduces the relative temporal variations (shown by the same color at different timings) and frequency dependence (shown by different colors at the same timing) and that the model systematically overestimates the attenuation by a factor of 3.7.

4. Discussion

Based on the analysis of MEX MARSIS and MAVEN SEP data, we observe the strongest correlations between the radio absorption and SEP fluxes at ∼1–2 MeV for ions and >100 keV for electrons. We note that the measured SEP ion fluxes at several tens of keV often include pickup oxygen ions of exospheric origin (Rahmati et al., 2014, 2015, 2017), which could potentially reduce the expected correlation because the energetic pickup oxygen ions do not typically precipitate to the nightside atmosphere. This "contamination" of pickup oxygen ions to SEP ion fluxes typically occurs only below ∼100 keV and is likely to be irrelevant to the increasing trend of the correlation from ∼100 keV to ∼1 MeV ions. In the model results, we find the peaks of attenuation around 50–60 km altitudes (Figure 5d), corresponding to the peak altitudes of the ion production rate by >100 keV electrons and ∼5 MeV protons during the December 2014 event (Figure 9 of Nakamura et al. (2022)). The observations and model results consistently suggest that >1 MeV for ions and >100 keV for electrons are the most effective energies of SEP particles that contribute to the 3–5 MHz radio absorption. Taken together with the data-model comparison of the time and frequency profiles of the December 2014 event (Figure 6), the model prediction is generally consistent with the relative temporal changes, radio frequency dependence, and SEP energy dependence of the observed radio absorption, but the absolute magnitude is systematically overestimated by a factor of ∼3.7.

We now discuss possible reasons for the systematic discrepancy between the observations and model results. We first consider uncertainties in the measured SEP fluxes. The sensitivity of the MAVEN SEP instrument could contain a systematic uncertainty just as any other particle instrument. We note that the factor of 3.7 overestimation of radio absorption (which is proportional to the electron density, see Equation 2) corresponds to a factor of $3.7^2 = 14$ overestimation of ion production rate (under photochemical equilibrium) and that of SEP flux if solely attributed to the SEP flux uncertainties. The overestimation by more than an order of magnitude appears too large for the sensitivity uncertainty given the good agreement between the measured and modeled fluxes of pickup oxygen (Rahmati et al., 2015, 2017), although a large systematic uncertainty of the sensitivity at relatively high energies cannot be ruled out completely.

In addition to the uncertainty of instrumental origin, SEP ion shadowing by Mars (Lillis et al., 2016) could result in anisotropic ion precipitation to the atmosphere, effectively reducing the precipitating ion flux compared to the upstream SEP flux. This geometric effect is proposed by Nakamura et al. (2022) as one of the main reasons for a factor of 2 discrepancy between the measured and modeled intensities of the diffuse aurora. However, to account for the large discrepancy inferred from the measured and modeled radio absorption by reducing the precipitating SEP ion flux, the vast majority of the incident angles must be shadowed by Mars *on average*, which seems incompatible with the observations (Lillis et al., 2016). Meanwhile, SEP electrons could be efficiently shielded by the induced and crustal magnetic fields of Mars due to their small gyroradii. Test particle simulations by Jolitz et al. (2021) suggest only 3% of the incident SEP electrons can reach the atmosphere. For the December 2014 event, roughly 20%–30% of the modeled radio absorption is attributed to SEP electron-induced ionization, and this portion of the modeled absorption could virtually vanish if we adopt the 3% transmission rate of SEP electrons to the atmosphere. Detailed modeling of the SEP ion and electron transport to the Martian atmosphere should be incorporated into a radio absorption model to achieve an accurate prediction.

Another source of systematic uncertainties is the electron-CO_2 collision frequency, which directly contributes to the attenuation computation (Equation 2). As already discussed in the previous section, the two experimentally derived formulations recommended by Witasse et al. (2001) have a small (∼30%) difference, which can only partially account for the factor of 3.7 discrepancy. We have not found strong evidence that the electron-CO_2 collision frequency is the main source of uncertainty.

Overall, we have not yet reached a definitive conclusion as to the source(s) of uncertainty causing the systematic discrepancy between the measured and modeled radio absorption. In any case, the data-model comparison presented in this study suggests that our ability to reproduce the observed radio absorption in the nightside ionosphere of Mars is far from complete even with MAVEN SEP measurements in Mars orbit and one of the state-of-the-art numerical models of the SEP-atmosphere interaction. In this respect, validation of the model results against other observations, for example, low-altitude electron density profiles derived from radio occultation (Withers et al., 2022), would be highly useful. Also, if we are to comprehensively assess the HF radio commu-

nication environment on Mars for future crew and spacecraft activities on the surface, we need to characterize the radio absorption not only on the nightside but also on the dayside. For the dayside radio absorption, a prediction model should include solar X-rays as an ionization source in addition to SEPs. It is desirable to develop a comprehensive Martian radio absorption model step by step complemented by analyses of data accumulated by ongoing and future observations of the Martian ionosphere and the drivers thereof.

5. Conclusions

Based on the analysis of radio wave absorption and SEP spectra observed by MEX and MAVEN, we quantitatively demonstrate that the radio absorption in the nightside ionosphere of Mars is clearly correlated with the upstream SEP fluxes. In the measured energy range, ∼200 keV electrons and ∼1–2 MeV ions have the strongest correlations with the observed radio absorption, suggesting their significant contribution to ionization at altitudes relevant to 3–5 MHz radio wave absorption. The effective energies inferred from the observations are consistent with the Monte Carlo model results conducted for the December 2014 event, which predict that most of the radio absorption occurs below 100 km altitudes with an absorption peak at ∼50–60 km. The model prediction also reproduces the relative temporal variations and frequency dependence of the observed radio absorption very well, but the absolute magnitude of the absorption is systematically overestimated by a factor of 3.7. This suggests that we need to identify and appropriately account for the systematic factor(s) ultimately causing the discrepancy in either the model or the observations, or both. We explore several possibilities including systematic uncertainties associated with the electron-CO_2 collision frequency, sensitivity of the MAVEN SEP instrument, and limited transport of SEPs to the atmosphere. The resolution of the model-observation discrepancy identified in this study is a crucial step toward developing a comprehensive model capable of assessing and predicting the HF radio absorption at Mars for future activities on the Martian surface.

Appendix A: Deriving Surface Echo Attenuation From MARSIS Data

Here we describe the data processing procedures to derive the surface echo attenuation that is analyzed in this paper to investigate the radio absorption in the Martian nightside ionosphere during solar energetic particle (SEP) events. We derive the surface echo attenuation by quantifying to what extent the measured echo power at a given time is weakened with respect to the reference echo power that is unaffected by the ionospheric absorption:

$$\text{Attenuation} = -10\log_{10}\left(\frac{P_{\text{mes}}}{P_{\text{ref}}}\right)\ \text{dB}, \tag{A1}$$

where P_{mes} is the measured echo power and P_{ref} is the reference echo power.

The first step is to extract the surface echo power from the Mars Advanced Radar for Subsurface and Ionospheric Sounding (MARSIS) Active Ionospheric Sounding (AIS) and subsurface mode data. From the AIS ionograms, we integrate the measured echo power over an apparent altitude range from −55 to 28 km to encompass the effective thickness of the ground trace due to signal dispersion and scattering (Němec et al., 2015). We derive the measured surface echo power for each of four frequency ranges: 3.0–3.5, 3.5–4.0, 4.0–4.5, and 4.5–5.0 MHz. From the subsurface mode data, we simply take the maximum signal strength in the measured time delay range as the surface echo power.

Figures A1 shows the surface echo power as a function of SEP electron flux and solar zenith angle (SZA) for the AIS (Figure A1a) and subsurface (Figure A1b) modes as well as the corresponding data densities (Figures A1c and A1d). The surface echo power clearly weakens at lower SZAs or for higher SEP electron fluxes. The former is caused by the reflection and absorption of radio waves by the dayside ionosphere (Nielsen et al., 2007), while the latter is due to enhanced radio absorption in the nightside ionosphere during SEP events and is the focus of this study. To characterize the nominal surface echo properties without the ionospheric effects and derive the reference echo power, we focus on the data obtained at SZA > 100° and when the SEP electron flux is lower than 10^2 cm^{-2} s^{-1} sr^{-1} in the following analysis.

For the quantitative analysis of the MARSIS surface echo power, we need to compensate for apparent echo power variations caused by the varying (a) spacecraft altitude (Mouginot et al., 2010; Nielsen et al., 2007), (b) spacecraft

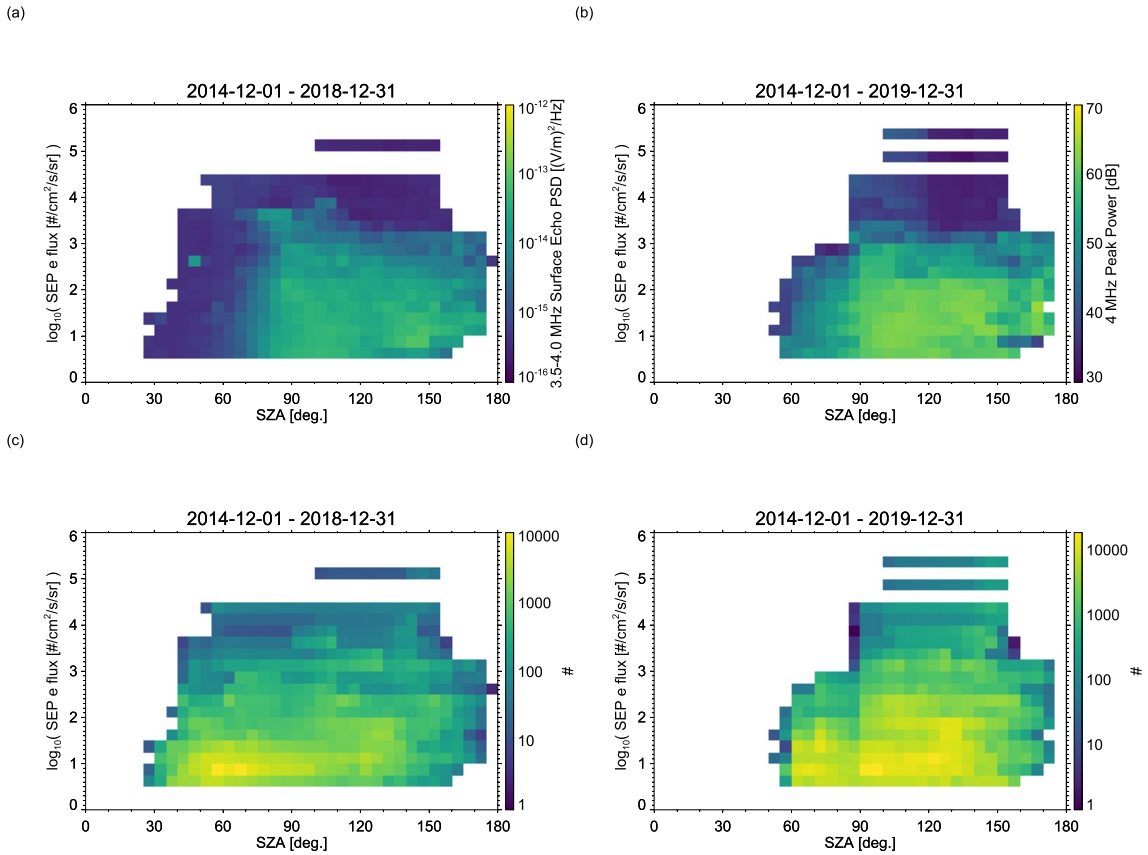

Figure A1. Average surface echo powers as a function of integrated Solar Energetic Particle electron flux and solar zenith angle derived from the Mars Advanced Radar for Subsurface and Ionospheric Sounding (a) Active Ionospheric Sounding and (b) subsurface modes along with (c, d) the number of data in each bin.

attitude (which has not been explicitly documented in the literature to our knowledge), and (c) surface reflectivity (Grima et al., 2012; Mouginot et al., 2010; Němec et al., 2015). The compensation procedures are presented in the following.

Figure A2 shows the surface echo power as a function of spacecraft altitude and MARSIS dipole antenna elevation angle (0° = horizontal, 90° = vertical). We observe systematic trends of weaker echo power at higher altitudes, corresponding to larger range attenuation for more distant targets. We also observe weaker echo power for larger antenna elevation angles. Given the dipole antenna directivity, the horizontal antenna direction is the most effective configuration for radar operation, and less power is transmitted to and received from the nadir for more inclined antenna configurations.

To compensate for the spacecraft altitude dependence, we utilize the radar equation for spherical waves reflected from a spherical surface Fresnel zone, Equation S.56 of Haynes (2020), $P_r = \frac{P_t G_t G_r \lambda^2 \Gamma}{(4\pi)^2 h^2} \frac{r^2}{(h+r)^2}$, where P_r is the received power, P_t is the transmitted power, G_t is the transmitter antenna gain, G_r is the receiver antenna gain, λ is the radio wavelength, Γ is the reflectivity at an interface, h is the altitude, and r is the spherical body radius. We take a reference altitude of 400 km, and derive the altitude-compensated surface echo power P_{400} from the measured surface echo power P at an altitude h,

$$P_{400} = P * \frac{(h * (h + R_M))^2}{((400\,\mathrm{km}) * ((400\,\mathrm{km}) + R_M))^2}, \tag{A2}$$

where R_M is the Mars radius. As we demonstrate later, the altitude dependence of the AIS surface echo power seen in Figure A2a1 is very well compensated by this equation. Meanwhile, the subsurface mode surface echo power seen in Figure A2b1 has a slightly weaker altitude dependence. We found that the altitude dependence of the subsurface mode data can be removed by the following compensation,

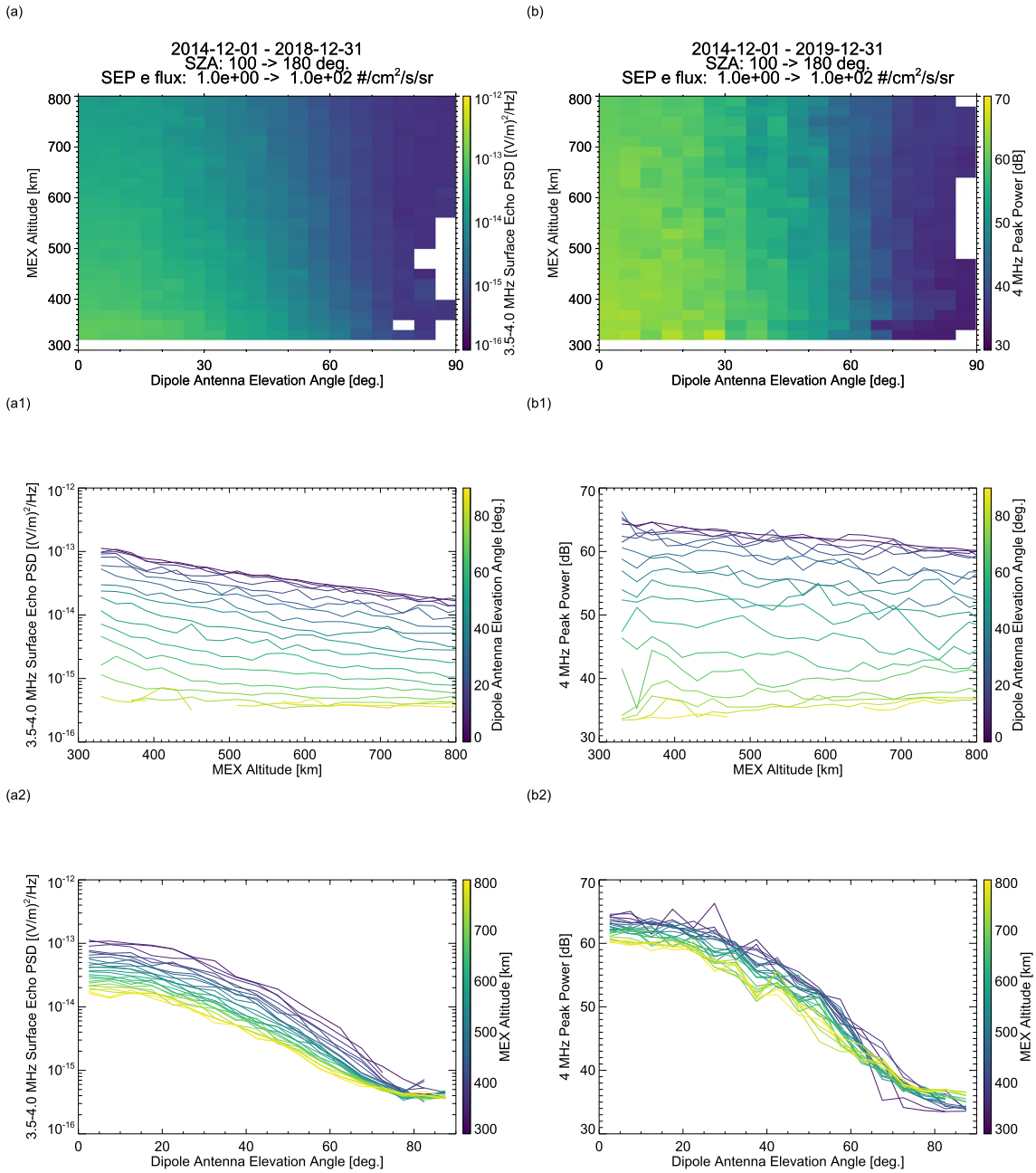

Figure A2. Average surface echo powers as a function of Mars Express altitude and Mars Advanced Radar for Subsurface and Ionospheric Sounding (MARSIS) dipole antenna elevation angle derived from the MARSIS (a) Active Ionospheric Sounding and (b) subsurface modes under the condition of solar zenith angle > 100° and Solar Energetic Particle electron flux $<10^2$ cm^{-2} s^{-1} sr^{-1}. The line plots (a1, a2, b1, and b2) show the same information as panels (a, b) in different formats.

$$P_{400} = P * \frac{(h * (h + R_M))^2}{((400\,\mathrm{km}) * ((400\,\mathrm{km}) + R_M))^2} \frac{400\,\mathrm{km}}{h}, \tag{A3}$$

where $\frac{400\,\mathrm{km}}{h}$ is an empirical correction factor. We apply Equation A2 to the AIS data and Equation A3 to the subsurface mode data.

In addition to the spacecraft altitude dependence, we compensate for the directivity of a half-wave dipole antenna (e.g., Silver, 1984) and normalize the surface echo power to the reference horizontal antenna direction by the following equation:

$$P_{400h} = P_{400} * \left[\cos\left(\frac{\pi}{2} * \cos\theta\right) / \sin\theta\right]^{-4}, \quad \text{(A4)}$$

where θ is the radio wave emission angle with respect to the antenna axis. For the nadir target, $\theta = 90°$—(dipole antenna elevation angle).

Figure A3 shows the surface echo power compensated for the spacecraft altitude and attitude variations in the same format as Figure A2. We observe the flat profiles of the compensated surface echo power independent of the spacecraft altitude and attitude for off-horizontal antenna angles up to ~45°, above which the apparent increase

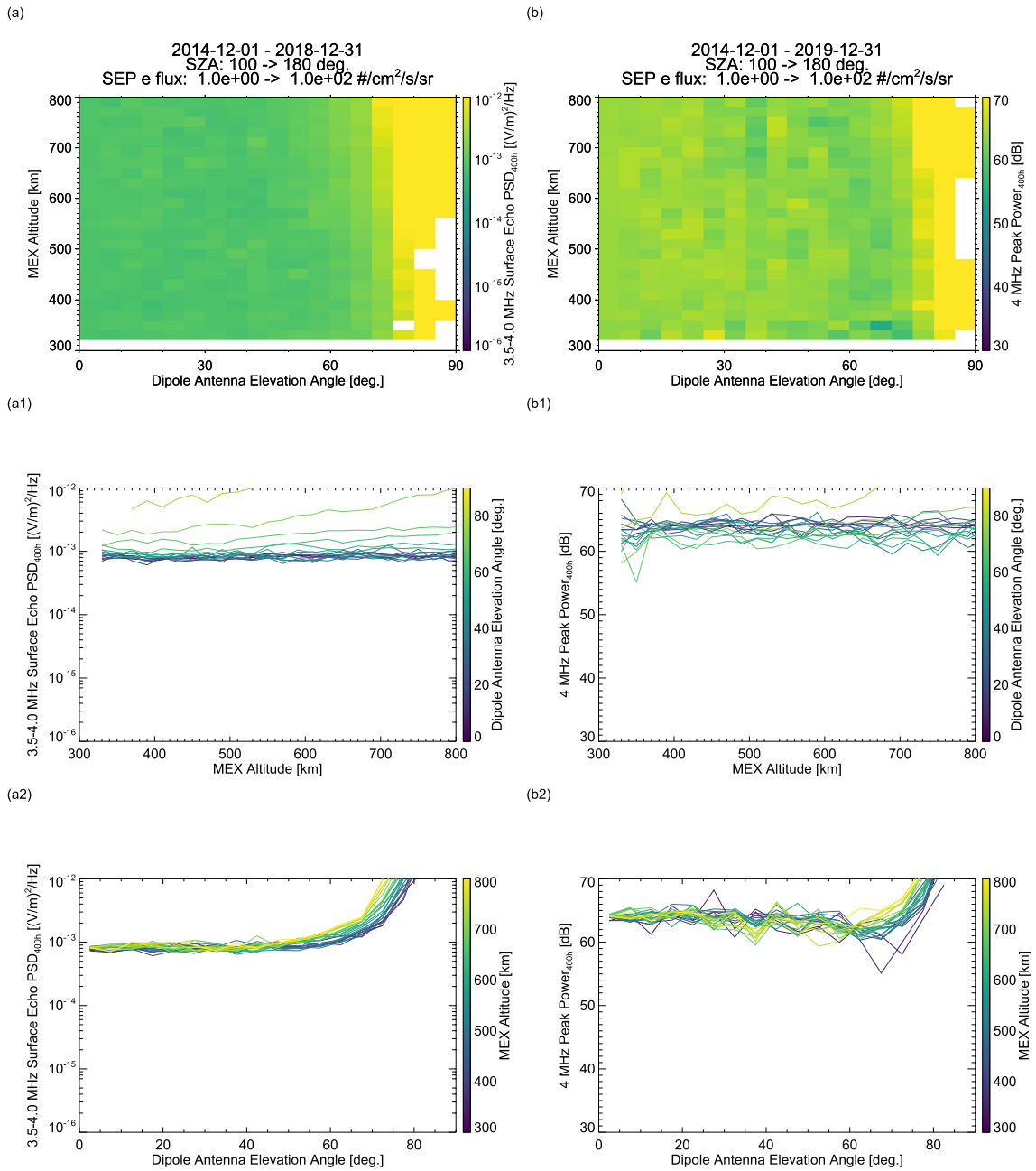

Figure A3. Average surface echo powers compensated for the spacecraft altitude and attitude as a function of Mars Express altitude and Mars Advanced Radar for Subsurface and Ionospheric Sounding dipole antenna elevation angle under the condition of solar zenith angle > 100° and Solar Energetic Particle electron flux $<10^2$ cm^{-2} s^{-1} sr^{-1} in the same format as Figure A2.

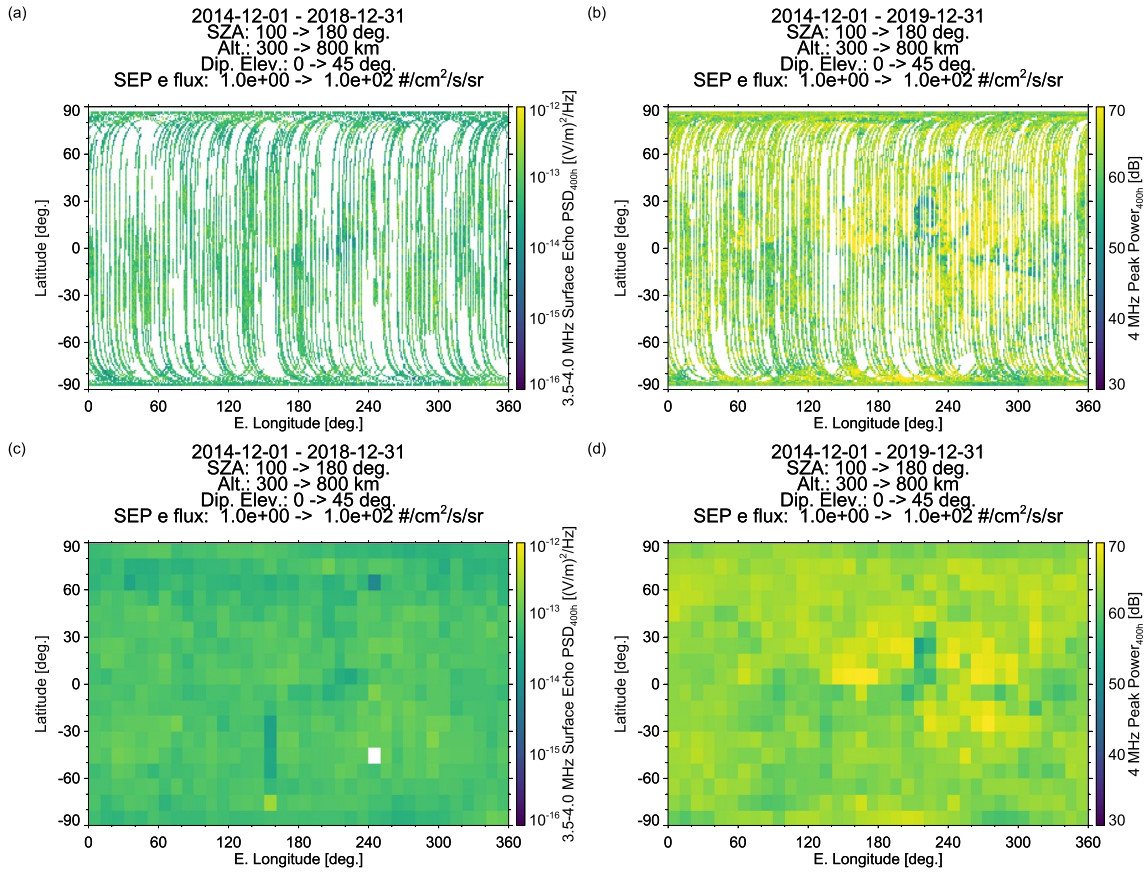

Figure A4. Average surface echo powers compensated for the spacecraft altitude and attitude as a function of longitude and latitude derived from the Mars Advanced Radar for Subsurface and Ionospheric Sounding (a) Active Ionospheric Sounding and (b) subsurface modes in 1° resolution and (c, d) those in 10° resolution under the condition of solar zenith angle > 100°, Solar Energetic Particle electron flux $<10^2$ cm^{-2} s^{-1} sr^{-1}, Mars Express altitude <800 km, and dipole antenna elevation angle <45°.

of the power is caused by the noise floor (cf. Figure A2). Therefore, we only use data obtained at altitudes of 300–800 km and dipole antenna elevation angles <45° to derive the reference surface echo power, P_{ref}.

Figures A4a and A4b show the geographic distributions of P_{400h} for the AIS and subsurface mode data, respectively. The geographic variations of surface reflectivity arise from variations in surface roughness and surface dielectric constant (Grima et al., 2012; Mouginot et al., 2010). Following Němec et al. (2015)'s methodology, we generate 10° × 10° maps of average P_{400h} (Figures A4c and A4d), and define the reference power, P_{ref}, for each 10° × 10° bin. Finally, we take the instantaneous P_{400h} as P_{mes} from the data obtained at altitudes of 300–500 km, SZAs > 100°, and dipole antenna elevation angles <30° to ensure a wide dynamic range of radio absorption under favorable radar operation conditions. For a given measurement of P_{mes}, P_{ref} is taken from the corresponding longitude-latitude bin, and the surface echo attenuation is computed according to Equation A1. We note that we tested the same analysis as it is described in the main text without the geographic compensation by taking P_{ref} from the global average, leading to no significant change in the radio absorption analysis results.

Data Availability Statement

The Mars Express MARSIS data used in this study are available at https://space.physics.uiowa.edu/plasma-wave/marsx/public-data.html, at https://pds-geosciences.wustl.edu/mex/, and at https://archives.esac.esa.int/psa/ftp/MARS-EXPRESS/MARSIS/. The MAVEN SEP data used in this study are available at https://pds-ppi.igpp.ucla.edu/mission/MAVEN/MAVEN/SEP.

Acknowledgments
YH is supported by JSPS KAKENHI Grant (22K14085). B.S.-C. acknowledges support through STFC Ernest Rutherford Fellowship ST/V004115/1 and M.L. through STFC Grant ST/W00089X/1. We thank Marco Cartacci for his assistance with the interpretation of the MARSIS subsurface mode data.

References

Ehresmann, B., Hassler, D. M., Zeitlin, C., Guo, J., Wimmer-Schweingruber, R. F., Matthiä, D., et al. (2018). Energetic particle radiation environment observed by rad on the surface of mars during the September 2017 event. *Geophysical Research Letters*, *45*(11), 5305–5311. https://doi.org/10.1029/2018GL077801

Espley, J. R., Farrell, W. M., Brain, D. A., Morgan, D. D., Cantor, B., Plaut, J. J., et al. (2007). Absorption of MARSIS radar signals: Solar energetic particles and the daytime ionosphere. *Geophysical Research Letters*, *34*(9), L09101. https://doi.org/10.1029/2006GL028829

Fowler, C. M., Andersson, L., Shaver, S. R., Thayer, J. P., Huba, J. D., Lillis, R., et al. (2017). MAVEN observations of ionospheric irregularities at Mars. *Geophysical Research Letters*, *44*(21), 10845–10854. https://doi.org/10.1002/2017GL075189

Fowler, C. M., Bonnell, J. W., Huba, J. D., Andersson, L., Espley, J., Benna, M., & Ergun, R. E. (2019). The statistical characteristics of small-scale ionospheric irregularities observed in the Martian ionosphere. *Journal of Geophysical Research: Space Physics*, *124*(7), 5874–5893. https://doi.org/10.1029/2019JA026677

Fowler, C. M., Bonnell, J. W., Xu, S., Benna, M., Elrod, M., McFadden, J., et al. (2020). First detection of kilometer-scale density irregularities in the Martian ionosphere. *Geophysical Research Letters*, *47*(22), e2020GL090906. https://doi.org/10.1029/2020GL090906

Grima, C., Kofman, W., Herique, A., Orosei, R., & Seu, R. (2012). Quantitative analysis of mars surface radar reflectivity at 20 MHz. *Icarus*, *220*(1), 84–99. https://doi.org/10.1016/j.icarus.2012.04.017

Gurnett, D., Huff, R., Morgan, D., Persoon, A., Averkamp, T., Kirchner, D., et al. (2008). An overview of radar soundings of the Martian ionosphere from the Mars Express spacecraft. *Advances in Space Research*, *41*(9), 1335–1346. https://doi.org/10.1016/j.asr.2007.01.062

Harada, Y., Gurnett, D. A., Kopf, A. J., Halekas, J. S., & Ruhunusiri, S. (2018). Ionospheric irregularities at Mars probed by MARSIS topside sounding. *Journal of Geophysical Research: Space Physics*, *123*(1), 1018–1030. https://doi.org/10.1002/2017JA024913

Harada, Y., Gurnett, D. A., Kopf, A. J., Halekas, J. S., Ruhunusiri, S., DiBraccio, G. A., et al. (2018). MARSIS observations of the Martian nightside ionosphere during the September 2017 solar event. *Geophysical Research Letters*, *45*(16), 7960–7967. https://doi.org/10.1002/2018GL077622

Haynes, M. S. (2020). Surface and subsurface radar equations for radar sounders. *Annals of Glaciology*, *61*(81), 135–142. https://doi.org/10.1017/aog.2020.16

Hunsucker, R. D. (1991). *Radio techniques for probing the terrestrial ionosphere* (Vol. 22). Springer Berlin Heidelberg. https://doi.org/10.1007/978-3-642-76257-4

Itikawa, Y. (1978). Momentum-transfer cross sections for electron collisions with atoms and molecules: Revision and supplement, 1977. *Atomic Data and Nuclear Data Tables*, *21*(1), 69–75. https://doi.org/10.1016/0092-640X(78)90004-9

Jolitz, R. D., Dong, C. F., Rahmati, A., Brain, D. A., Lee, C. O., Lillis, R. J., et al. (2021). Test particle model predictions of SEP electron transport and precipitation at mars. *Journal of Geophysical Research: Space Physics*, *126*(8), e2021JA029132. https://doi.org/10.1029/2021JA029132

Jordan, R., Picardi, G., Plaut, J., Wheeler, K., Kirchner, D., Safaeinili, A., et al. (2009). The Mars express MARSIS sounder instrument. *Planetary and Space Science*, *57*(14–15), 1975–1986. https://doi.org/10.1016/j.pss.2009.09.016

Kataoka, R. (2022). Chapter 3 - Technological vulnerability and statistics. In R. Kataoka (Ed.), *Extreme space weather* (pp. 65–92). Elsevier. https://doi.org/10.1016/B978-0-12-822537-0.00002-8

Larson, D. E., Lillis, R. J., Lee, C. O., Dunn, P. A., Hatch, K., Robinson, M., et al. (2015). The MAVEN solar energetic particle investigation. *Space Science Reviews*, *195*(1), 153–172. https://doi.org/10.1007/s11214-015-0218-z

Lee, C. O., Hara, T., Halekas, J. S., Thiemann, E., Chamberlin, P., Eparvier, F., et al. (2017). MAVEN observations of the solar cycle 24 space weather conditions at Mars. *Journal of Geophysical Research: Space Physics*, *122*(3), 2768–2794. https://doi.org/10.1002/2016JA023495

Lee, C. O., Jakosky, B. M., Luhmann, J. G., Brain, D. A., Mays, M. L., Hassler, D. M., et al. (2018). Observations and impacts of the 10 September 2017 solar events at Mars: An overview and synthesis of the initial results. *Geophysical Research Letters*, *45*(17), 8871–8885. https://doi.org/10.1029/2018GL079162

Lester, M., Sanchez-Cano, B., Potts, D., Lillis, R., Cartacci, M., Bernardini, F., et al. (2022). The impact of energetic particles on the Martian ionosphere during a full solar cycle of radar observations: Radar blackouts. *Journal of Geophysical Research: Space Physics*, *127*(2), e2021JA029535. https://doi.org/10.1029/2021JA029535

Lillis, R. J., Lee, C. O., Larson, D., Luhmann, J. G., Halekas, J. S., Connerney, J. E. P., & Jakosky, B. M. (2016). Shadowing and anisotropy of solar energetic ions at Mars measured by MAVEN during the March 2015 solar storm. *Journal of Geophysical Research: Space Physics*, *121*(4), 2818–2829. https://doi.org/10.1002/2015JA022327

Mayyasi, M., Narvaez, C., Benna, M., Elrod, M., & Mahaffy, P. (2019). Ion-neutral coupling in the upper atmosphere of mars: A dominant driver of topside ionospheric structure. *Journal of Geophysical Research: Space Physics*, *124*(5), 3786–3798. https://doi.org/10.1029/2019JA026481

Melnik, O., & Parrot, M. (1999). Propagation of electromagnetic waves through the Martian ionosphere. *Journal of Geophysical Research*, *104*(A6), 12705–12714. https://doi.org/10.1029/1999JA900100

Mendillo, M., Pi, X., Smith, S., Martinis, C., Wilson, J., & Hinson, D. (2004). Ionospheric effects upon a satellite navigation system at Mars. *Radio Science*, *39*(2), 1–11. https://doi.org/10.1029/2003RS002933

Millour, E., Forget, F., Spiga, A., Vals, M., Zakharov, V., Montabone, L., et al. (2018). *The mars climate database (version 5.3) from mars express to exomars scientific workshop*. ESA-ESAC.

Morgan, D. D., Diéval, C., Gurnett, D. A., Duru, F., Dubinin, E. M., Fränz, M., et al. (2014). Effects of a strong ICME on the Martian ionosphere as detected by Mars express and Mars Odyssey. *Journal of Geophysical Research: Space Physics*, *119*(7), 5891–5908. https://doi.org/10.1002/2013JA019522

Morgan, D. D., Gurnett, D. A., Kirchner, D. L., Winningham, J. D., Frahm, R. A., Brain, D. A., et al. (2010). Radar absorption due to a corotating interaction region encounter with Mars detected by MARSIS. *Icarus*, *206*(1), 95–103. https://doi.org/10.1016/j.icarus.2009.03.008

Mouginot, J., Pommerol, A., Kofman, W., Beck, P., Schmitt, B., Herique, A., et al. (2010). The 3–5 MHz global reflectivity map of mars by MARSIS/Mars express: Implications for the current inventory of subsurface H_2O. *Icarus*, *210*(2), 612–625. https://doi.org/10.1016/j.icarus.2010.07.003

Nakamura, Y., Leblanc, F., Terada, N., Hiruba, S., Murata, I., Nakagawa, H., et al. (2023). Numerical prediction of changes in atmospheric chemical compositions during a solar energetic particle event on mars. *Journal of Geophysical Research: Space Physics*, *128*(12), e2022JA031250. https://doi.org/10.1029/2022JA031250

Nakamura, Y., Terada, N., Koyama, S., Yoshida, T., Karyu, H., Terada, K., et al. (2023). Photochemical and radiation transport model for extensive use (PROTEUS). *Earth Planets and Space*, *75*(1), 140. https://doi.org/10.1186/s40623-023-01881-w

Nakamura, Y., Terada, N., Leblanc, F., Rahmati, A., Nakagawa, H., Sakai, S., et al. (2022). Modeling of diffuse auroral emission at mars: Contribution of MeV protons. *Journal of Geophysical Research: Space Physics*, *127*(1), e2021JA029914. https://doi.org/10.1029/2021JA029914

Němec, F., Morgan, D. D., Diéval, C., & Gurnett, D. A. (2015). Intensity of nightside MARSIS AIS surface reflections and implications for low-altitude ionospheric densities. *Journal of Geophysical Research: Space Physics*, *120*(4), 3226–3239. https://doi.org/10.1002/2014JA020888

Němec, F., Morgan, D. D., Diéval, C., Gurnett, D. A., & Futaana, Y. (2014). Enhanced ionization of the Martian nightside ionosphere during solar energetic particle events. *Geophysical Research Letters*, *41*(3), 793–798. https://doi.org/10.1002/2013GL058895

Němec, F., Morgan, D. D., Gurnett, D. A., & Duru, F. (2010). Nightside ionosphere of Mars: Radar soundings by the Mars express spacecraft. *Journal of Geophysical Research*, *115*(E12), E12009. https://doi.org/10.1029/2010JE003663

Nielsen, E., Morgan, D., Kirchner, D., Plaut, J., & Picardi, G. (2007). Absorption and reflection of radio waves in the Martian ionosphere. *Planetary and Space Science*, *55*(7–8), 864–870. https://doi.org/10.1016/j.pss.2006.10.005

Rahmati, A., Cravens, T. E., Nagy, A. F., Fox, J. L., Bougher, S. W., Lillis, R. J., et al. (2014). Pickup ion measurements by MAVEN: A diagnostic of photochemical oxygen escape from Mars. *Geophysical Research Letters*, *41*(14), 4812–4818. https://doi.org/10.1002/2014GL060289

Rahmati, A., Larson, D. E., Cravens, T. E., Lillis, R. J., Dunn, P. A., Halekas, J. S., et al. (2015). MAVEN insights into oxygen pickup ions at Mars. *Geophysical Research Letters*, *42*(21), 8870–8876. https://doi.org/10.1002/2015GL065262

Rahmati, A., Larson, D. E., Cravens, T. E., Lillis, R. J., Halekas, J. S., McFadden, J. P., et al. (2017). MAVEN measured oxygen and hydrogen pickup ions: Probing the Martian exosphere and neutral escape. *Journal of Geophysical Research: Space Physics*, *122*(3), 3689–3706. https://doi.org/10.1002/2016JA023371

Ramstad, R., Holmström, M., Futaana, Y., Lee, C. O., Rahmati, A., Dunn, P., et al. (2018). The September 2017 SEP event in context with the current solar cycle: Mars express ASPERA-3/IMA and MAVEN/SEP observations. *Geophysical Research Letters*, *45*(15), 7306–7311. https://doi.org/10.1029/2018GL077842

Reames, D. V. (2013). The two sources of solar energetic particles. *Space Science Reviews*, *175*(1), 53–92. https://doi.org/10.1007/s11214-013-9958-9

Rishbeth, H., & Garriott, O. K. (1969). *Introduction to ionospheric physics*. Academic Press.

Sánchez-Cano, B., Blelly, P.-L., Lester, M., Witasse, O., Cartacci, M., Orosei, R., et al. (2019). Origin of the extended Mars radar blackout of September 2017. *Journal of Geophysical Research: Space Physics*, *124*(0), 4556–4568. https://doi.org/10.1029/2018JA026403

Schneider, N. M., Deighan, J. I., Jain, S. K., Stiepen, A., Stewart, A. I. F., Larson, D., et al. (2015). Discovery of diffuse aurora on Mars. *Science*, *350*(6261), aad0313. https://doi.org/10.1126/science.aad0313

Schneider, N. M., Jain, S. K., Deighan, J., Nasr, C. R., Brain, D. A., Larson, D., et al. (2018). Global aurora on Mars during the September 2017 Space weather event. *Geophysical Research Letters*, *45*(15), 7391–7398. https://doi.org/10.1029/2018GL077772

Schunk, R. W., & Nagy, A. F. (1980). Ionospheres of the terrestrial planets. *Reviews of Geophysics*, *18*(4), 813–852. https://doi.org/10.1029/RG018i004p00813

Silver, S. (1984). *Microwave antenna theory and design* (No. (19)). Iet.

Whitten, R. C., & Poppoff, I. G. (1971). *Fundamentals of aeronomy*. John Wiley and Sons, Inc.

Witasse, O., Nouvel, J.-F., Lebreton, J.-P., & Kofman, W. (2001). Hf radio wave attenuation due to a meteoric layer in the atmosphere of Mars. *Geophysical Research Letters*, *28*(15), 3039–3042. https://doi.org/10.1029/2001GL013164

Withers, P. (2011). Attenuation of radio signals by the ionosphere of Mars: Theoretical development and application to MARSIS observations. *Radio Science*, *46*(2), RS2004. https://doi.org/10.1029/2010RS004450

Withers, P., Felici, M., Mendillo, M., Vogt, M. F., Barbinis, E., Kahan, D., et al. (2022). Observations of high densities at low altitudes in the nightside ionosphere of mars by the maven radio occultation science experiment (ROSE). *Journal of Geophysical Research: Space Physics*, *127*(11), e2022JA030737. https://doi.org/10.1029/2022JA030737

Yoshida, T., Aoki, S., Ueno, Y., Terada, N., Nakamura, Y., Shiobara, K., et al. (2023). Strong depletion of ^{13}C in CO induced by photolysis of CO_2 in the Martian atmosphere, calculated by a photochemical model. *The Planetary Science Journal*, *4*(3), 53. https://doi.org/10.3847/PSJ/acc030

Zeitlin, C., Hassler, D. M., Guo, J., Ehresmann, B., Wimmer-Schweingruber, R. F., Rafkin, S. C. R., et al. (2018). Analysis of the radiation hazard observed by rad on the surface of mars during the September 2017 solar particle event. *Geophysical Research Letters*, *45*(12), 5845–5851. https://doi.org/10.1029/2018GL077760